



Nanoscale

**Nanomechanics of Self-Assembled Surfactants Revealed by
Frequency-Modulation Atomic Force Microscopy**

Journal:	<i>Nanoscale</i>
Manuscript ID	NR-ART-01-2022-000369.R1
Article Type:	Paper
Date Submitted by the Author:	21-Feb-2022
Complete List of Authors:	Umeda, Kenichi; Kanazawa University Kobayashi, Kei; Kyoto University, Department of Electronic Science and Engineering Yamada, Hirofumi; Kyoto University, Department of Electronic Science and Engineering

SCHOLARONE™
Manuscripts

Nanomechanics of Self-Assembled Surfactants Revealed by Frequency-Modulation Atomic Force Microscopy

Kenichi Umeda¹⁻³, Kei Kobayashi³, and Hirofumi Yamada³

¹ *Nano Life Science Institute (WPI-NanoLSI),*

Kanazawa University, Kakuma-machi, Kanazawa, Ishikawa, 920-1192, Japan.

² *PRESTO/JST, 4-1-8 Honcho, Kawaguchi, Saitama 332-0012, Japan.*

³ *Department of Electronic Science and Engineering,*

Kyoto University, Katsura, Nishikyo, Kyoto 615-8510, Japan.

Prof. Hirofumi Yamada (corresponding author)

Department of Electronic Science and Engineering, Kyoto University

E-mail: umeda.k@piezo.kuee.kyoto-u.ac.jp

Surfactants play a critical role in bottom-up nanotechnologies due to their peculiar nature of controlling the interfacial energy. Since their operational mechanism originates from the molecular-scale formation and disruption processes of molecular assemblies (i.e., micelles), conventional static-mode atomic force microscopy has made a significant contribution to unravel the detailed molecular pictures. Recently, we have successfully developed a local solvation measurement technique based on three-dimensional frequency-modulation atomic force microscopy, whose spatial resolution is not limited by jump-to-contact. Here, using this novel technique, we investigate molecular nanomechanics in the formation and disruption processes of micelles formed on a hydrophobic surface. Furthermore, an experiment employing a hetero-nanostructure reveals that the nanomechanics depends on the form of the molecular assembly. Namely, the hemifusion and disruption process are peculiar to the micellar surface and causes a higher energy dissipation than the monolayer surface. The technique established in this study will be used as a generic technology for further development of bottom-up nanotechnologies.

Introduction

Surfactant molecular assemblies, such as micelles and films, are observed in various fields because of their basic functionality of modifying interfacial energy; common examples include detergents and cell membranes comprising lipid bilayers. They play a crucial role in bottom-up nanofabrication technologies of functional nanoarchitectures, e.g., the separation of single-wall carbon nanotubes;¹ the exfoliation of graphene;^{2,3} nanosculpting of designable materials with complex topologies;⁴ and fabrication of nanoporous/microporous metal–organic framework adsorbents,⁵ metal nanocrystals,^{6,7} quantum dots,⁸ liquid crystals,⁹ and catalysts for batteries.¹⁰ Hence, obtaining detailed molecular pictures of the micellar structures and formation-and-disruption processes is crucial to further develop functional nanoarchitectures. To date, static-mode atomic force microscopy (SM-AFM) has successfully revealed micelles' structures at the nanoscale level.¹¹⁻¹⁹ However, jump-to-contact has prevented an accurate analysis of their formation-and-disruption processes.^{12,14,15,20-22}

Over the past decade, we have initiated the visualization of 3D hydration structures²³⁻³¹ and surface charge distributions^{28,30-32} at the solid–liquid interface using ultra-low noise frequency-modulation AFM (FM-AFM). Since this method allows the use of stiff cantilevers, information about the tip–sample interaction at all the distances can be evaluated without being impaired by jump-to-contact. Previously, we succeeded in the first 3D force mapping measurement on surfactant micelles, which visualized the surface charge distribution on hemicylindrical micelles (hemimicelles) formed on a hydrophobic graphite surface.²⁸ However, most of the past studies have

investigated uniform micellar surfaces, and in addition, they have not taken into account the existence of micelles on the tip and the elastic force by compression of the micelles.

Therefore, in this study, we first characterized FM-AFM force mapping results on surfactant micelles by considering the effects mentioned above, which illuminate the detailed molecular mechanism of the micellar formation and disruption processes. We then discuss the force mapping results of micelles in different phase states, which demonstrates how the different fluidity is reflected in experiments. However, to truly understand the molecular mechanism, an experiment employing a hetero-nanostructure with the same tip condition is essential because changing the phase state affects the tip micelles as well as the sample micelles. Furthermore, the applications to practical nanoarchitectures would necessitate the measurement of the local micellar structure that depends on the local surface properties. Therefore, we performed force map measurements of a hetero-nanostructure comprising hemicylindrical micelles and monolayers, demonstrating that the micelles' viscoelastic structures can be quantitatively evaluated by theoretically analyzing the force and the simultaneously obtained dissipation and mean deflection data.

Methods

Sample and solutions. We used two types of typical ionic surfactants (Fig. S1 depicts their molecular structures), i.e., a anionic surfactant, sodium dodecyl sulfate [SDS, $\text{CH}_3(\text{CH}_2)_{11}\text{OSO}_3^-\text{Na}^+$] (Wako Pure Chemical Industries, Ltd.: 20765), and a cationic surfactant, cetyltrimethylammonium bromide [CTAB, $\text{CH}_3(\text{CH}_2)_{15}\text{N}^+(\text{Br}^-)(\text{CH}_3)_3$] (Nacalai Tesque: 07906-82). We prepared a 30 mM SDS aqueous solution and a 1 mM CTAB aqueous solution from ultrapure water (Merck), whose concentrations are greater than the individual critical micelle concentrations (CMCs) (8.3 mM for SDS and CTAB, 0.96 mM for CTAB³³, Supporting Information A). As a substrate, highly-oriented pyrolytic graphite (ZYA grade, NT-MDT) was used. Immediately after the cleavage using Scotch tape in air, the imaging solution was dropped onto the surface, followed by the FM-AFM experiments.

FM-AFM Setup. The details of the instrumentation and force map measurement are described in our previous reports.^{27,30,31} We used a customized commercial AFM head (Shimadzu: SPM-9600) with a home-built digital PXI controller based on a field-programmable gate array board programmed by LabVIEW (National Instruments: NI PXI-8196, NI PXI-7833R) and a home-built FM detector circuit.³⁴ To achieve quantitative and reproducible force measurements in liquid environments, we employed a photothermal excitation setup.³⁵ All the experiments were conducted in a temperature-regulated enclosure (Mitsubishi Electric Engineering Company, Ltd.: CN-40A), which can maintain a constant temperature of 293 or 298 K with a variation of ± 0.1 K. We used

PPP-NCHAuD (Nanosensors) cantilevers with the typical spring constant and resonance frequency in solutions of 30 N/m and 140 kHz, respectively. Immediately prior to each experiment, organic contaminations on the tip were removed by irradiation using a UV-ozone cleaner (Filgen: UV253) for a few hours. We set the oscillation amplitude at approximately 0.5 nm peak-to-peak, which is lower than the thickness of the hemimicelles.

Force Map Measurements. We simultaneously acquired 2D vertical images of the frequency shift (Δf), excitation voltage, and cantilever mean deflection (Δz). At each lateral pixel, their signals versus distance curves were recorded by translating the tip toward the sample using a triangular waveform signal of 11 Hz, which corresponds to a tip velocity of about 40 nm/s. When Δf reached a predetermined threshold value (Δf_{thr}), the approach was immediately stopped, then the tip was retracted to the original position while acquiring the signals. The post-processing was conducted using a home-built program developed in Visual Studio (Microsoft) as described below. The 2D vertical maps were smoothed via a Gaussian kernel filter with the standard deviation of 0.18 nm (x) and 0.01 nm (z). The force profiles were created from the averaged Δf profiles using Sader's method.³⁶ The acquired excitation voltage maps were converted to energy dissipation (P_{tip}) maps using an equation, which considers the coupling with the Δf signal (Supporting Information B).

Results & Discussion

Disruption Process of Micelles. Hemimicelles are formed on a graphite surface^{11,37,38} while being templated by an underneath epitaxial monolayer (Fig. 1a).^{13,20,37,39} First, we performed a Δf map measurement on the hemimicelles in a 30 mM SDS solution with Δf_{thr} of 0.8 kHz (Fig. 1b,c), almost same value used in the previous study.²⁸ The image depicts a cross-section of the hemicylindrical molecular assembly with the thickness approximately the same as its molecular length of 2 nm as previously reported.²⁸ The green region in the bottom of the image is an area without data, and the border between the area with and without data represents the distance at which Δf reached Δf_{thr} , namely, the “apparent surface”. After conducting an extensive analysis of the numerous force map data, we were able to classify the force (Δf) curves into three regimes (Fig. 1d). The schematics deduced from the experimental results are summarized in Fig. 2. Since the surfactant micelles are formed on the hydrophilic surfaces as well,^{13,40-42} it is highly possible that they would also be formed on the SiO₂/Si tip surface.¹⁹ As discussed later, we assumed that spherical micelles were formed on the tip due to the significantly small radius of curvature (Supporting Information C).¹³

Prior to contact between the micelles on the tip and sample, an exponential repulsive force regime was observed (regime E), which is caused by the electric double layer (EDL) force (Fig. 2a), as already discussed in previous studies.^{20,22,28} This regime was followed by a micellar elastic compression regime (regime C) of ~2 nm in thickness (Fig. 2b).^{12,14,15,17,20-22,43} Although Δf linearly

increased as the distance was decreased in this regime, the Hertz theory, which predicts a power law of $3/2$,⁴⁴ can be fitted to the force versus distance curve converted from the Δf curve, which provides the Young's modulus of the micelles, as discussed later. The boundary between the EDL and Hertz regimes can be estimated from the crossover point between the fitted linear line and exponential curve. Following this regime, the hemifusion of the micelles was observed (regime D) with a breakthrough Δf of 0.35 kHz, which corresponds to the force of 0.1–0.3 nN (Fig. 2c). After that, a significant attractive force due to the meniscus force, followed by a steep increase in Δf , was observed during the disruption process of the micelles (Fig. 2d).

We gradually increased Δf_{thr} from 0.5 to 2.8 kHz (Fig. 3), which correspond approximately to the force of 0.4 and 1.2 nN, respectively. When Δf_{thr} was 0.5 kHz (Fig. 3a), the vertical image almost similar to Fig. 1(c) was obtained. This means that if Δf_{thr} is insufficient to disrupt the micelles, the process follows a direct path from Fig. 2d to Fig. 2f. However, when it was increased to 2 kHz, discontinuous jumps appeared in the Δf_{thr} border line, which is apparent surface (Fig. 3b). We then further increased it to 2.8 kHz, and six multiple solvation peaks with intervals of 0.52 nm appeared, and the apparent thickness of the micelles was increased to 5 nm (see the height difference of the apparent micelle from the real graphite in Figs. 3c–e). These multiple peaks can be attributed to the surfactant molecules solvated on the surface in a fluid-like micelle, where the observation mechanism of the oscillatory peaks seems to be similar to that of room-temperature ionic liquids.⁴⁵ In our previous study, we already reported the observation of solvation layers inside the micelle,²⁸ but only two layers were observed. This result demonstrated that FM-AFM has an advantage of

acquiring the solvation measurement over SM-AFM.

Taking into account the regime C, we estimated the total tip–sample distance at the contact of their micelles to be 7 nm, which corresponds to the total thickness of the hemicylinder and bilayer. This means that if Δf_{thr} is high enough to disrupt the micelles, the process follows the path from Fig. 2d to Fig. 2f through Fig. 2e. Although it might be possible that a permanently adsorbed additional layer exists, it is hardly disrupted without damaging the tip and sample surfaces.

Micelles in Different Phase States. In the above experiments, we discussed only the disruption processes using SDS and next discuss the reformation processes as well. The micelles have a physical property of the Krafft temperature, which is defined as the melting temperature of the micelles, and hence a different formation process can be observed in either a liquid crystal (LC) or gel phase. Those of SDS and CTAB are 288 K⁴⁶ and 293–298 K,^{46,47} respectively, which predicts SDS micelles in a LC phase and CTAB micelles in either the LC or gel phase at room temperature. To compare these different phases, we conducted force mapping experiments on CTAB hemimicelles at 298 and 293 K. While topographic images of two types of micelles did not show a notable difference, the Δf map images showed a significant difference. A Δf map image at 298 K showed an image feature similar to that obtained in the SDS solution, which implied the micellar formation in the LC phase (Fig. 4a,b). We noticed that the hemimicellar surface was slightly translocated upward during the retraction compared to the approach process, but the main features were not significantly altered. In contrast, although a hemicylindrical structure was also observed at

293 K, the distinct breakthrough force was not observed and hence the micellar structure exhibited an entirely bright contrast (Fig. 4c). Furthermore, the retraction image showed a much greater hysteresis than that in the LC phase (Fig. 4d), which implies a highly viscous solid-like state.

Additionally, we examined the simultaneously acquired P_{tip} images in Figs. 4e–h because its signal is commonly utilized for evaluating the viscoelasticity^{48,49} and atomic-and-molecular fluctuations.^{50,51} We found that a significant difference appears in the P_{tip} maps. In the LC phase (Fig. 4e,f), the bright contrast appeared only in the vicinity of the surface, while in the gel phase (Fig. 4g,h), the bright regions extends to the onset of the intermicellar interaction, which is quite similar to the corresponding Δf image. The significantly lower P_{tip} observed in the LC phase indicates that the mechanism of the micelle hemifusion and dissociation processes is a reversible and purely conservative phenomenon. Since the micelle form is thermally equilibrated with the monomers in the bulk solution, there is no intrinsic free energy change associated with the formation and disruption processes. Therefore, when the balance of the equilibrium reaction is perturbed by the tip interaction, the micellar morphological change would also in principle spontaneously occur without an energy loss. Since the inside of the micellar shell in the LC phase behaves like a fluid, once the tip is penetrated into the micelles, the high P_{tip} is unlikely to be caused unless the tip does not interact with the strongly adsorbed solvation layers. In contrast, since those in the gel phase behaves like a solid, the molecules are not equilibrated and remained on the surface even under the tip interaction, which causes the significantly higher P_{tip} accompanied by an irreversible disruption process. These results are consistent with previous studies that showed

viscosity⁵² as well as Young's modulus⁵³ in a gel phase exhibits more than one order of magnitude greater than those in a fluid phase. Note that although SM-AFM is also utilized for evaluating the energy loss during the entire force profile, FM-AFM has the advantage that it can be evaluated at the moment of the hemifusion-and-dissociation processes. By exploiting the FM-AFM advantage, we successfully revealed that the increase in P_{tip} reflects the phase state and surfactant topology.

To quantitatively analyze the data, we retrieved a laterally averaged force profile using a force conversion method³⁶ on either the top or valley of the hemimicelles (Figs. 4i-l). The distinct attractive force was only visible in the LC phase possibly due to the meniscus force, and the force profile in the gel phase showed a monotonic increase. The P_{tip} profiles in the LC phase showed a small peak in the elastic deformation regime (see green arrow), which means that compression of the micelles is a slightly dissipated structural change. The P_{tip} curve in the gel phase showed a steep increase at the onset of the force rise, followed by a monotonic increase (discussed later in detail). In the gel phase, since the molecules in the micelles are not equilibrated with those in the bulk solution, the micellar hemifusion causes such a large P_{tip} due to the irreversible structural change, which likely to cause a polymer-brush-like force profile.^{16,17}

Micelle Hetero-nanostructure. In the gel phase, we could observe a hetero-nanostructure consisting of the hemimicelles that partially exposes monolayers in the same experiment (Fig. 5a).^{11,37,38} Therefore, we further applied this technique to a spontaneously formed hetero-nanostructure in order to exclude the tip effects and better understand its use in practical

applications. We observed a large step line (height: 2.7 nm) across the image (see the blue arrows), corresponding to the eight graphite layers. A significant increase in P_{tip} was observed on the hemimicellar region relative to monolayer region (Fig. 5b). We also observed a noticeable increase in Δz on the monolayer region (Fig. 5c).

To investigate their nature in more detail, we performed a vertical force map measurement across the boundary. The Δf map in Fig. 5d illustrated a slightly brighter contrast on the monolayer than on the hemimicellar region. In contrast, the P_{tip} map in Fig. 5e depicted the monolayer region with a considerably brighter contrast than that observed in the hemimicellar region. Conversely, the Δz map in Fig. 5f showed the hemimicellar region with an obviously brighter contrast regardless of the extremely weak signal variations. Although the corresponding retraction images also showed a similar contrast as the approach images (Fig. 5g-i), in the Δf and P_{tip} maps (Fig. 5g,h), they exhibited a hysteretic feature only on the H regions.

To perform a quantitative analysis, we extracted the averaged profiles from each region (Supporting Information E, Fig. S6, and Fig. 6a), and converted the Δf to force curves (Fig. 6b,c). A distinct hysteresis was observed on the hemimicellar region, whereas it was not obvious on the monolayer region. Note that the hydration structures in water generally do not exhibit such a strong hysteresis as well as P_{tip} due to the equilibrium system (Supporting Information F, Fig. S7). The profiles on the hemimicelles were almost equivalent to those shown in Fig. 4k,l. On the monolayer,

the transition between the C and D regimes was not very distinct in the profiles, which indicated that the tip seamlessly penetrates into the surfactant gel (Figs. 2g–i).

By fitting the elastic regimes to the Hertz contact model equation, we estimated their Young's modulus to be the same value of 3 MPa (Supporting Information G), where we considered the bottom-effect correction because recent studies have demonstrated that this effect is important for the quantitative estimation of the Young's modulus of a thin material on a rigid substrate.^{44,54} This result implies that apparently high stiffness observed on the monolayer mainly originate from the topological difference. This value is just slightly smaller than 10 MPa reported for the lipid bilayer⁴⁴ possibly due to the low degree of molecular packing. Note that in one special case, a bare tip was realized in experiments, which was the result of the use of a double chain surfactant having a significantly low CMC (Supporting Information H).

Figs. 6d,e depict a steep increase in P_{tip} at the onset of the micelle hemifusion on the hemimicellar region, whereas only a moderate monotonic increase was observed on the monolayer. In the Δz curves on the hemimicellar region shown in Fig. 6f, a minute snap-in with a 10-pm depth was observed concurrently with the micelle hemifusion (see the purple arrow). However, this occurrence is comparable to the attractive force of 300 pN due to the high stiffness of the cantilever.

Interestingly, in spite of such a strong force, it did not appear in the FM-AFM force profile (Fig. 6b). Since the Δf signal does not reflect the absolute value of the force, but instead the dynamic equilibrium force at the resonance frequency and proportional to the derivative of the force, the transient force is not reflected in principle. This means that it originates from a nonequilibrium

meniscus force by the micellar hemifusion, which is not synchronized with the tip oscillation.

In association with the micelle compression, the tip apex penetrated into the surfactant gel, and P_{tip} discontinuously increased due to the significant viscosity in the gel. In the retraction process, P_{tip} gradually decreased (Fig. 2d) and the pull-off event by the micellar dissociation occurred 2 nm far away from the snap-in event (Fig. 2f), which implies that the micelles bridged between the tip and sample was stretched by the tip movement. Meanwhile, on the monolayer, such a discontinuous increase of P_{tip} as well as the hysteresis was not observed, which implies a purely conservative interaction.

By fitting the P_{tip} curves in the disruption regime using a hydrodynamic equation, we estimated their viscosities to be 0.3–0.4 Pa·s on both regions (Supporting Information I), approximately similar to that of a lipid bilayer (0.2 Pa·s).⁵⁵ These results indicated that the P_{tip} contrast observed in Figs. 5b,e,h originates from the differences in the thickness of the disrupted molecular gels bound to the sample surfaces.

There are some relevant methods, such as force modulation⁵⁶ and bimodal AFM,^{44,57,58} which are also powerful techniques for easily acquiring the viscoelastic properties concurrently with the topographic imaging. In solution, however, the 3D force map measurement is essential because the viscoelastic property three-dimensionally distributes in the solvation structures. Our results clearly demonstrated that FM-AFM can not only illustrate three-dimensional structures but also provide quantitative information about their molecular-scale viscoelastic properties via the theoretical analyses. To the best of our knowledge, we believe that this is also the first report about the

comparative analysis of site-specific Δf , P_{tip} , and Δz maps simultaneously acquired by liquid FM-AFM.

Conclusions

In this study, we disclose the nanomechanics of the formation and disruption processes of surfactant micelles in solutions via FM-AFM force map measurements. By precisely analyzing the vertical force maps and curves, we found that the force curves can be classified into three force regimes: exponential EDL, elastic compression, and micelle disruption regimes. We also measured the force maps on a hetero-nanostructure and found that a significant P_{tip} was observed only on the hemimicelle due to the hemifusion and disruption between the micelles on the tip and sample. We also quantitatively estimated the Young's modulus and viscosity of the micelles via theoretical analyses with a sufficient consideration for the substrate effect. Information from this study will be used to investigate the molecular-scale mechanisms of various bottom-up technologies to facilitate the creation of functional nanoarchitectures.

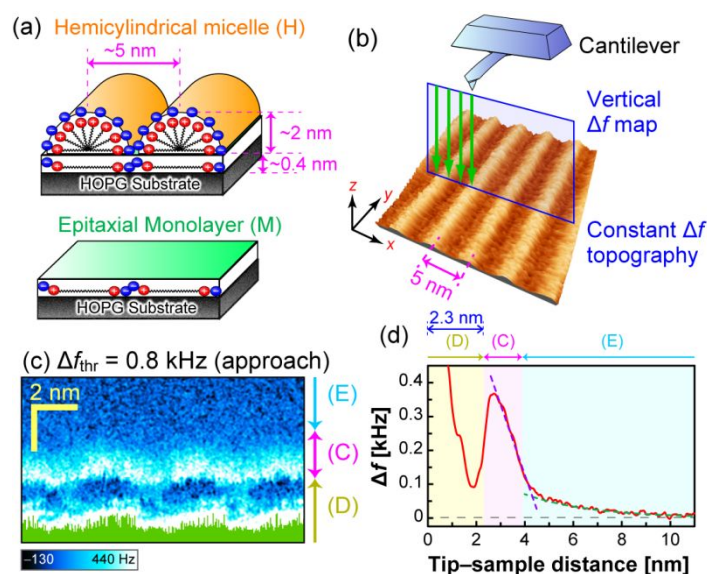


Fig. 1 (a) Schematics of two types of surfactant structures observed in the experiments; hemimicelles (H) and epitaxial monolayer (M). (b) Schematic of the force map measurement and a typical constant frequency shift (Δf) topography of a hemicylindrical micelle. (c,d) Vertical Δf map obtained in a 30 mM SDS solution with Δf_{thr} of 0.8 kHz in the approach direction. (d) Laterally averaged Δf curves reconstructed from the vertical maps shown in Fig. 1c. The dark purple and green broken lines indicate fitted linear and exponential curves for identifying the force regimes, respectively.

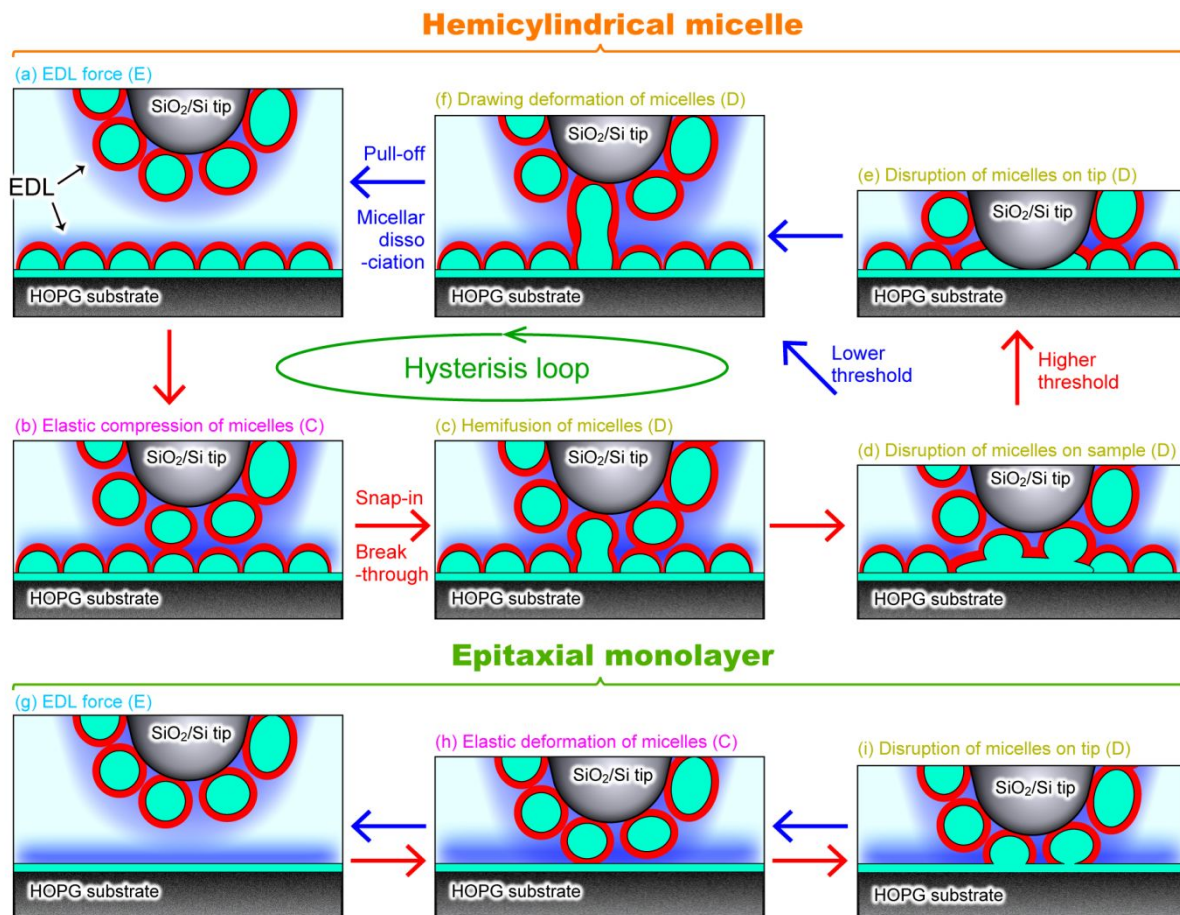


Fig. 2 (a–i) Schematics of the molecular disruption/reformation processes of the hemicylindrical surfactant micelles (**a–f**) and monolayer (**g–i**) structures revealed by FM-AFM. The red and blue arrows show the approach and retraction processes, respectively. We assumed that the formation of spherical micelles on the tip; however, a monolayer or bilayer like structure is plausible for the case in the gel phase. The main difference between the LC and gel phase are, regardless of the tip interaction, whether the molecular assembly is a fluid-like structure in a thermal equilibrium system or not.

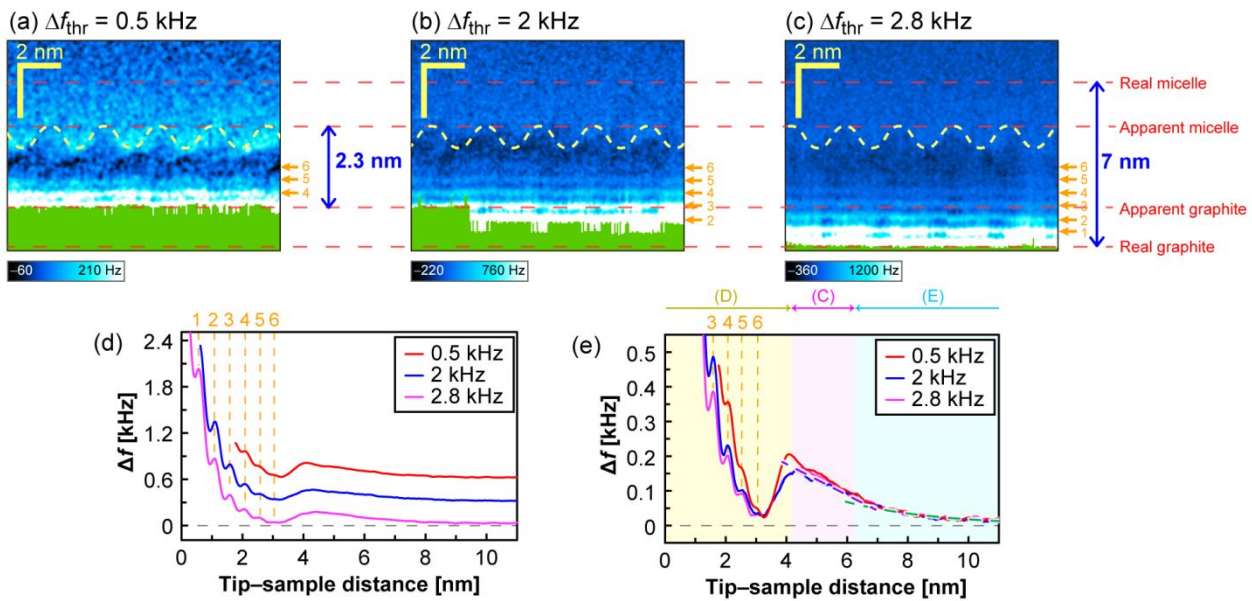


Fig. 3 (a–c) Vertical Δf map obtained in a 30 mM SDS solution with Δf_{thr} of 0.8 **(a)**, 2 **(b)**, and 2.8 **(c)** kHz in the approach direction, respectively. **(d,e)** Distance dependence of Δf curves laterally averaged across the hemimicelles in the vertical maps shown in Fig. 3a–c **(d)** and its vertically magnified graph **(e)**. The dark purple and green broken lines indicate fitted linear and exponential curves, respectively. Note that we fitted the exponential curve to the experimental result only far from the surface by assuming the Debye length to be 3 nm predicted from the experimental condition (Supporting Information D). The curve in the C regime was fitted to the linear curve, and the crossover point between the fitted linear line and exponential curve was used to define the border of the C and E regimes.

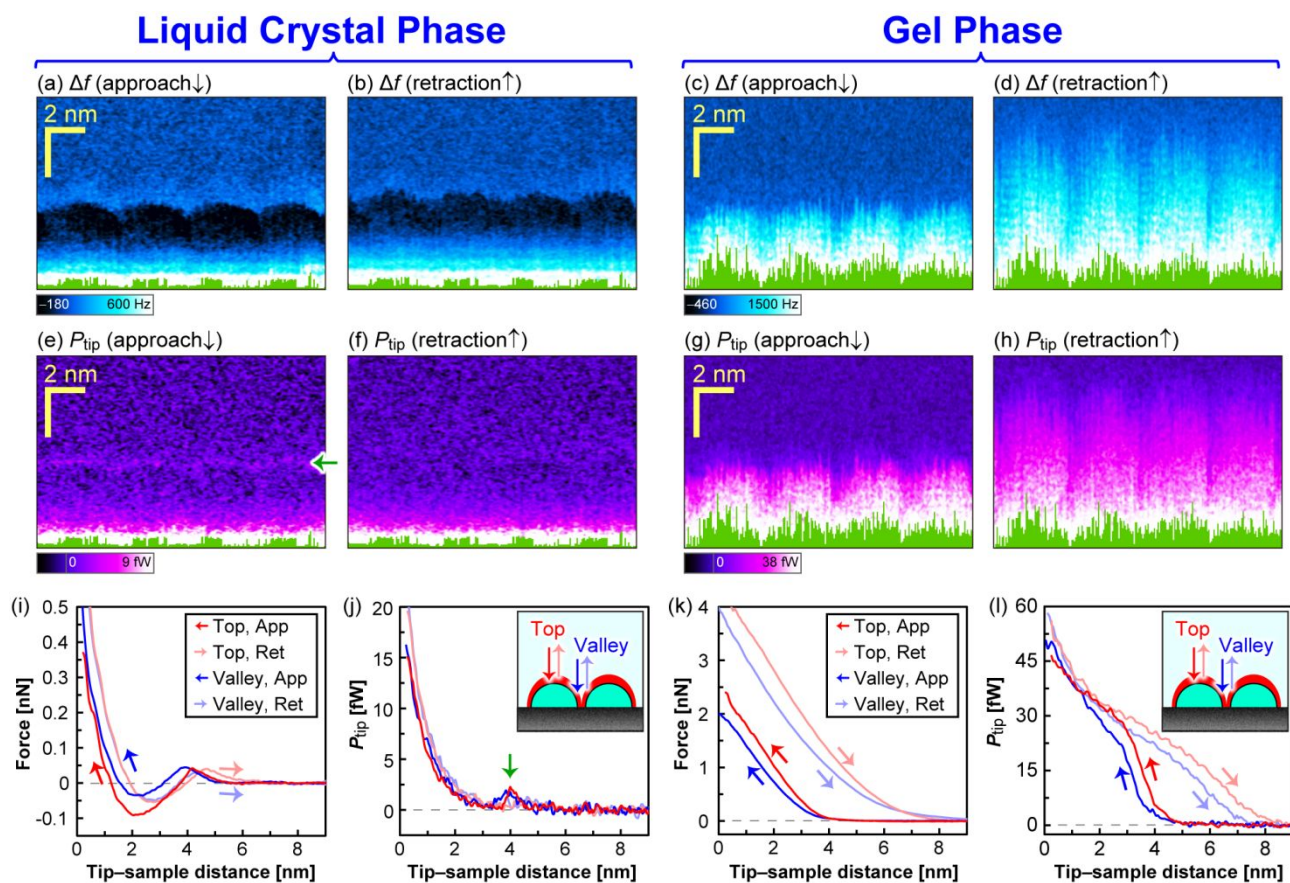


Fig. 4 (a–h) Vertical Δf (a–d) and P_{tip} (e–h) maps in the approach (a,c,e,g) and retraction (b,d,f,h) directions obtained on CTAB micelles in the liquid crystal phase (298 K) (a,b,e,f) and gel phase (293 K) (c,d,g,h). (i–l) Force (i,k) and P_{tip} (j,l) curves obtained by averaging the curves extracted from the top (red curve) and valley (blue curve) of the hemicylinders at 298 (i,j) and 293 K (k,l). The definition of top and valley position is depicted in the inset of (j,l). In (e,j), the green arrow indicates a small peak due to the deformation regime with slightly dissipated process.

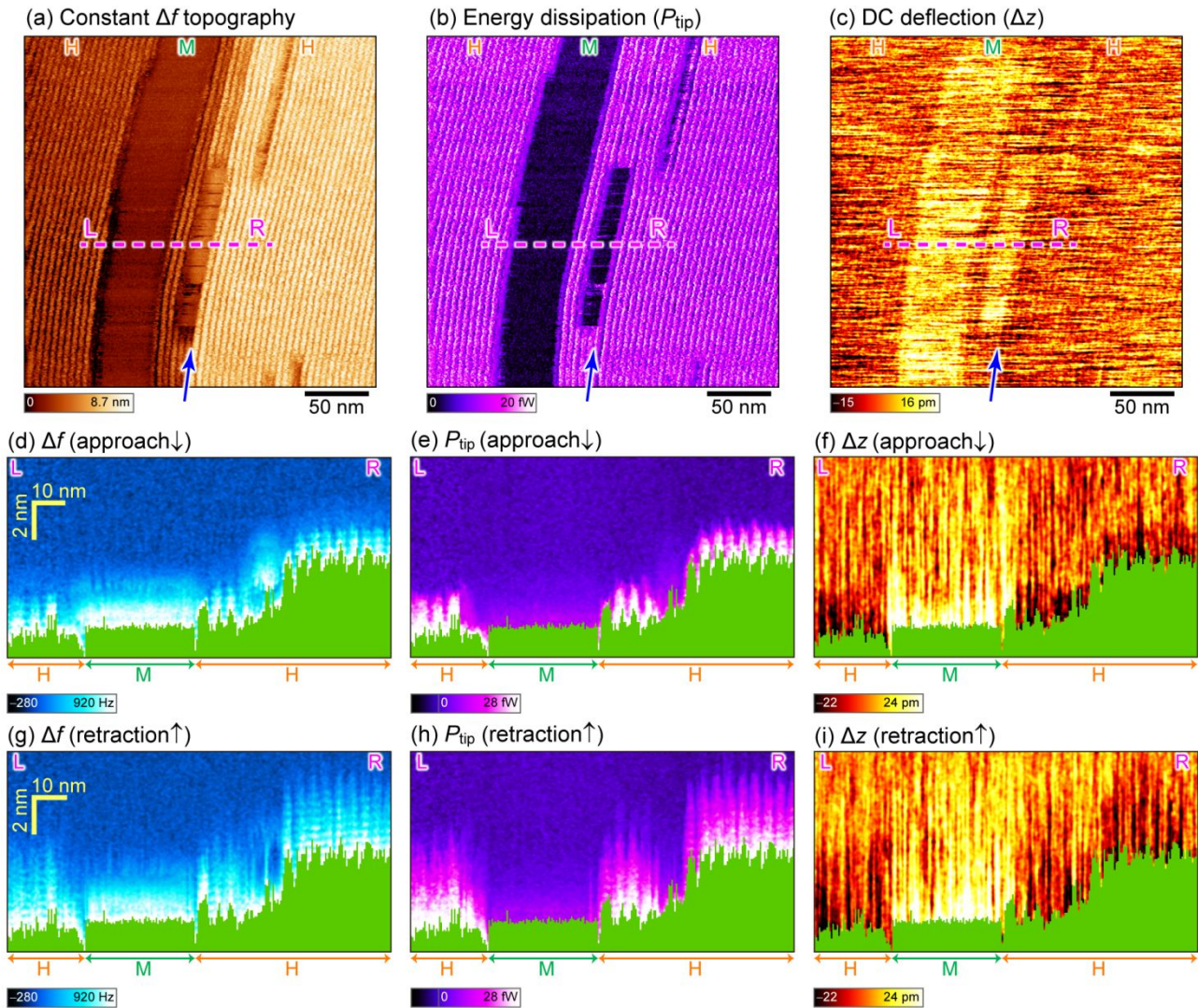


Fig. 5 (a–c) Constant Δf topography (a) and simultaneously obtained P_{tip} (b) and Δz (c) map images on the hemicylindrical (H) and monolayer (M) regions in a 1 mM CTAB solution at 293 K. In (a–c), the blue arrows indicate a step line of the graphite substrate. (d–i) Vertical Δf (d), P_{tip} (e), and Δz (f) maps in the approach (d–f) and retraction (g–i) directions simultaneously obtained at the purple broken lines in (a–c).

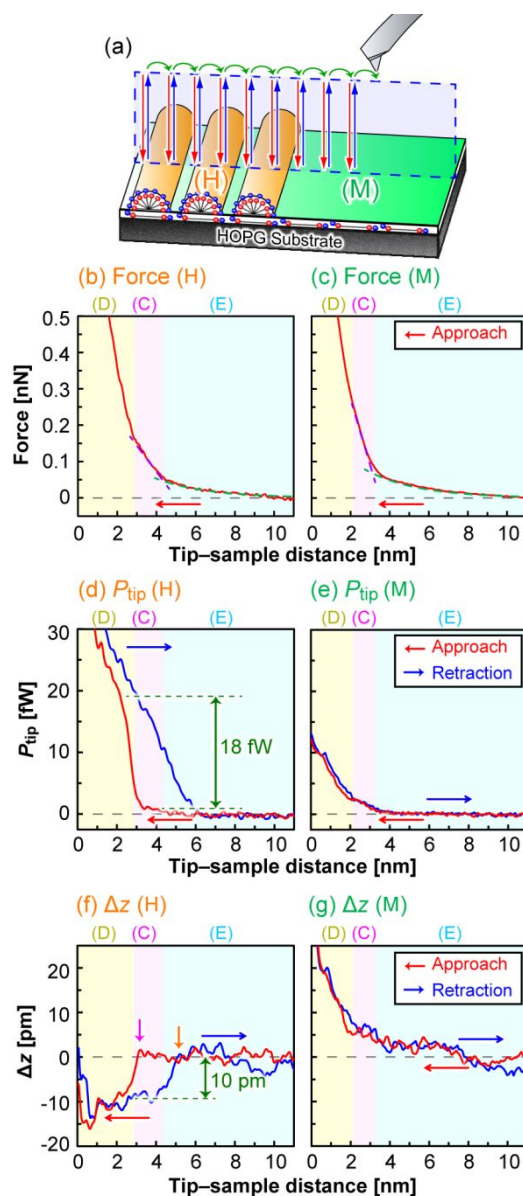


Fig. 6 (a) Schematic of the force map measurement on a hetero-nanostructure. (b–g) Laterally averaged force (b,c), P_{tip} (d,e), and Δz (f,g) curves obtained in the hemicylindrical (H) (b,d,f) and monolayer (M) (c,e,g) regions shown in Fig. 5. The red and blue curves represent the profiles in the approach and retraction directions, respectively. In (b,c), the purple and green broken lines indicate the fitted linear and exponential curves, respectively, which were used to define the force regimes. In (f), the positions of the snap-in and pull-off events are indicated by the purple and orange arrows, respectively.

Conflicts of interest

There are no conflicts of interest to declare.

Acknowledgments

This work was supported by KAKENHI, Japan Society for the Promotion of Science [Grant Nos. 19K15409; 21K04849 (to K.U.), 19H02598 (to K.K), and 17H06122 (to H.Y.)]; Foundation Advanced Technology Institute; the Murata Science Foundation; and JST Nanotech Career-up Alliance (to K.U.), and JST PRESTO [Grant No JPMJPR20E3] (to K.U.).

Author contributions

K. U. performed the FM-AFM imaging and analyzed the data. K. K. developed the AFM instruments and electronics. H. Y. supervised the whole study. All authors have discussed the results and been involved in writing the manuscript.

References

- 1 N. K. Subbaiyan, S. Cambre, A. N. G. Parra-Vasquez, E. H. Haroz, S. K. Doorn and J. G. Duque, *ACS Nano*, 2014, **8**, 1619-1628.
- 2 A. A. Green and M. C. Hersam, *Nano Lett.*, 2009, **9**, 4031-4036.
- 3 M. Lotya, Y. Hernandez, P. J. King, R. J. Smith, V. Nicolosi, L. S. Karlsson, F. M. Blighe, S. De, Z. Wang, I. T. McGovern, G. S. Duesberg and J. N. Coleman, *J. Am. Chem. Soc.*, 2009, **131**, 3611-3620.
- 4 T. Gibaud, E. Barry, M. J. Zakhary, M. Henglin, A. Ward, Y. S. Yang, C. Berciu, R. Oldenbourg, M. F. Hagan, D. Nicastro, R. B. Meyer and Z. Dogic, *Nature*, 2012, **481**, 348-351.
- 5 G. Lu, S. Z. Li, Z. Guo, O. K. Farha, B. G. Hauser, X. Y. Qi, Y. Wang, X. Wang, S. Y. Han, X. G. Liu, J. S. DuChene, H. Zhang, Q. C. Zhang, X. D. Chen, J. Ma, S. C. J. Loo, W. D. Wei, Y. H. Yang, J. T. Hupp and F. W. Huo, *Nat. Chem.*, 2012, **4**, 310-316.
- 6 Y. M. Zhai, J. S. DuChene, Y. C. Wang, J. J. Qiu, A. C. Johnston-Peck, B. You, W. X. Guo, B. DiCiaccio, K. Qian, E. W. Zhao, F. Ooi, D. H. Hu, D. Su, E. A. Stach, Z. H. Zhu and W. D. Wei, *Nat. Mater.*, 2016, **15**, 889-895.
- 7 X. C. Ye, C. Zheng, J. Chen, Y. Z. Gao and C. B. Murray, *Nano Lett.*, 2013, **13**, 765-771.
- 8 J. Yang, T. Ling, W. T. Wu, H. Liu, M. R. Gao, C. Ling, L. Li and X. W. Du, *Nat. Commun.*, 2013, **4**, 1695.

- 9 X. G. Wang, D. S. Miller, E. Bukusoglu, J. J. de Pablo and N. L. Abbott, *Nat. Mater.*, 2016, **15**, 106-112.
- 10 S. H. Oh, R. Black, E. Pomerantseva, J. H. Lee and L. F. Nazar, *Nat. Chem.*, 2012, **4**, 1004-1010.
- 11 M. H. Chen, I. Burgess and J. Lipkowski, *Surf. Sci.*, 2009, **603**, 1878-1891.
- 12 E. J. Wanless and W. A. Ducker, *J. Phys. Chem.*, 1996, **100**, 3207-3214.
- 13 J. F. Liu and W. A. Ducker, *J. Phys. Chem. B*, 1999, **103**, 8558-8567.
- 14 L. M. Grant, F. Tiberg and W. A. Ducker, *J. Phys. Chem. B*, 1998, **102**, 4288-4294.
- 15 R. E. Lamont and W. A. Ducker, *J. Am. Chem. Soc.*, 1998, **120**, 7602-7607.
- 16 I. Sokolov, G. Zorn and J. M. Nichols, *Analyst*, 2016, **141**, 1017-1026.
- 17 B. L. Micklavzina and M. L. Longo, *Langmuir*, 2017, **33**, 10483-10491.
- 18 B. L. Micklavzina, S. W. Zhang, H. He and M. L. Longo, *Langmuir*, 2017, **33**, 2122-2132.
- 19 J. J. Hamon, R. F. Tabor, A. Striolo and B. P. Grady, *Langmuir*, 2018, **34**, 7223-7239.
- 20 S. Manne, J. P. Cleveland, H. E. Gaub, G. D. Stucky and P. K. Hansma, *Langmuir*, 1994, **10**, 4409-4413.
- 21 W. A. Ducker and L. M. Grant, *J. Phys. Chem.*, 1996, **100**, 11507-11511.
- 22 K. Hu and A. J. Bard, *Langmuir*, 1997, **13**, 5418-5425.
- 23 A. Labuda, K. Kobayashi, K. Suzuki, H. Yamada and P. Grütter, *Phys. Rev. Lett.*, 2013, **110**, 066102.
- 24 D. Martin-Jimenez, E. Chacon, P. Tarazona and R. Garcia, *Nat. Commun.*, 2016, **7**, 12164.

- 25 H. Söngen, B. Reischl, K. Miyata, R. Bechstein, P. Raiteri, A. L. Rohl, J. D. Gale, T. Fukuma and A. Kühnle, *Phys. Rev. Lett.*, 2018, **120**, 116101.
- 26 T. Fukuma, B. Reischl, N. Kobayashi, P. Spijker, F. F. Canova, K. Miyazawa and A. S. Foster, *Phys. Rev. B*, 2015, **92**, 155412.
- 27 K. Umeda, K. Kobayashi, T. Minato and H. Yamada, *Phys. Rev. Lett.*, 2019, **122**, 116001.
- 28 K. Suzuki, K. Kobayashi, N. Oyabu, K. Matsushige and H. Yamada, *J. Chem. Phys.*, 2014, **140**, 054704.
- 29 M. R. Uhlig, D. Martin-Jimenez and R. Garcia, *Nat. Commun.*, 2019, **10**, 2606.
- 30 K. Umeda, L. Zivanovic, K. Kobayashi, J. Ritala, H. Kominami, P. Spijker, A. S. Foster and H. Yamada, *Nat. Commun.*, 2017, **8**, 2111.
- 31 K. Umeda, K. Kobayashi, T. Minato and H. Yamada, *J. Phys. Chem. Lett.*, 2020, **11**, 1343-1348.
- 32 K. Umeda, K. Kobayashi, N. Oyabu, K. Matsushige and H. Yamada, *Nanotechnology*, 2015, **26**, 285103.
- 33 P. Carpena, J. Aguiar, P. Bernaola-Galvan and C. C. Ruiz, *Langmuir*, 2002, **18**, 6054-6058.
- 34 K. Kobayashi, H. Yamada, H. Itoh, T. Horiuchi and K. Matsushige, *Rev. Sci. Instrum.*, 2001, **72**, 4383-4387.
- 35 K. Kobayashi, H. Yamada and K. Matsushige, *Rev. Sci. Instrum.*, 2011, **82**, 033702.
- 36 J. E. Sader and S. P. Jarvis, *Appl. Phys. Lett.*, 2004, **84**, 1801-1803.
- 37 N. B. Holland, M. Ruegsegger and R. E. Marchant, *Langmuir*, 1998, **14**, 2790-2795.

- 38 I. Burgess, C. A. Jeffrey, X. Cai, G. Szymanski, Z. Galus and J. Lipkowski, *Langmuir*, 1999, **15**, 2607-2616.
- 39 H. Kawasaki, M. Syuto and H. Maeda, *Langmuir*, 2001, **17**, 8210-8216.
- 40 W. A. Ducker and E. J. Wanless, *Langmuir*, 1999, **15**, 160-168.
- 41 Y. L. Chen, S. Chen, C. Frank and J. Israelachvili, *J. Colloid Interface Sci.*, 1992, **153**, 244-265.
- 42 S. B. Velegol, B. D. Fleming, S. Biggs, E. J. Wanless and R. D. Tilton, *Langmuir*, 2000, **16**, 2548-2556.
- 43 S. Xu, M. Chen, E. Cholewa, G. Szymanski and J. Lipkowski, *Langmuir*, 2007, **23**, 6937-6946.
- 44 V. G. Gisbert and R. Garcia, *ACS Nano*, 2021, **15**, 20574-20581.
- 45 K. Amano, Y. Yokota, T. Ichii, N. Yoshida, N. Nishi, S. Katakura, A. Imanishi, K. Fukui and T. Sakka, *Phys. Chem. Chem. Phys.*, 2017, **19**, 30504-30512.
- 46 C. Vautier-Giongo and B. L. Bales, *J. Phys. Chem. B*, 2003, **107**, 5398-5403.
- 47 J. Z. Manojlovic, *Thermal Science*, 2012, **16**, S631-S640.
- 48 K. Voitchovsky, J. J. Kuna, S. A. Contera, E. Tosatti and F. Stellacci, *Nat. Nanotechnol.*, 2010, **5**, 401-405.
- 49 A. Raman, S. Trigueros, A. Cartagena, A. P. Z. Stevenson, M. Susilo, E. Nauman and S. A. Contera, *Nat. Nanotechnol.*, 2011, **6**, 809-814.
- 50 A. A. Farrell, T. Fukuma, T. Uchihashi, E. R. Kay, G. Bottari, D. A. Leigh, H. Yamada and

S. P. Jarvis, *Phys. Rev. B*, 2005, **72**, 125430.

51 N. Oyabu, P. Pou, Y. Sugimoto, P. Jelinek, M. Abe, S. Morita, R. Perez and O. Custance, *Phys. Rev. Lett.*, 2006, **96**, 106101.

52 G. J. Amador, D. van Dijk, R. Kieffer, M. E. Aubin-Tam and D. Tam, *Proc. Natl. Acad. Sci. USA*, 2021, **118**, e2100156118.

53 O. Et-Thakafy, N. Delorme, C. Gaillard, C. Meriadec, F. Artzner, C. Lopez and F. Guyomarc'h, *Langmuir*, 2017, **33**, 5117-5126.

54 N. Gavara and R. S. Chadwick, *Nat. Nanotechnol.*, 2012, **7**, 733-736.

55 Y. L. Wu, M. Štefl, A. Olzyńska, M. Hof, G. Yahioğlu, P. Yip, D. R. Casey, O. Ces, J. Humpolíčková and M. K. Kuimova, *Phys. Chem. Chem. Phys.*, 2013, **15**, 14986-14993.

56 T. Igarashi, S. Fujinami, T. Nishi, N. Asao and K. Nakajima, *Macromolecules*, 2013, **46**, 1916-1922.

57 M. Kocun, A. Labuda, W. Meinhold, I. Revenko and R. Proksch, *ACS Nano*, 2017, **11**, 10097-10105.

58 E. T. Herruzo, A. P. Perrino and R. Garcia, *Nat. Commun.*, 2014, **5**, 3126.